

# MUSE Deep-Fields: The Ly $\alpha$ Luminosity Function in the Hubble Deep Field South at $2.91 < z < 6.64$ .

Alyssa B. Drake<sup>1</sup>, Bruno Guiderdoni<sup>1</sup>, J  r  my Blaizot<sup>1</sup>, Lutz Wisotzki<sup>2</sup>, Edmund Christian Herenz<sup>2</sup>, Thibault Garel<sup>1</sup>, Johan Richard<sup>1</sup>, Roland Bacon<sup>1</sup>, David Bina<sup>5</sup>, Sebastiano Cantalupo<sup>3</sup>, Thierry Contini<sup>5,6</sup>, Mark den Brok<sup>3</sup>, Takuya Hashimoto<sup>1</sup>, Raffaella Anna Marino<sup>3</sup>, Roser Pell  5, Joop Schaye<sup>4</sup>, Kasper B. Schmidt<sup>2</sup>

<sup>1</sup>Univ Lyon, Univ Lyon1, Ens de Lyon, CNRS, Centre de Recherche Astrophysique de Lyon UMR5574, F-69230, Saint-Genis-Laval, France

<sup>2</sup>Leibniz-Institut f  r Astrophysik Potsdam (AIP), An der Sternwarte 16, 14482 Potsdam, Germany

<sup>3</sup>ETH Z  rich, Institute for Astronomy, Department of Physics, Wolfgang-Pauli-Strasse 27, 8093 Z  rich, Switzerland

<sup>4</sup>Leiden Observatory, P.O. Box 9513, NL-2300 RA Leiden, The Netherlands

<sup>5</sup>IRAP, Institut de Recherche en Astrophysique et Plan  tologie, CNRS, 14 avenue   douard Belin, 31400 Toulouse, France,

<sup>6</sup>Universit   de Toulouse, UPS-OMP, 31400 Toulouse, France

13 September 2016

## ABSTRACT

We present the first estimate of the Ly $\alpha$  luminosity function using blind spectroscopy from the *Multi Unit Spectroscopic Explorer*, MUSE, in the *Hubble Deep Field South*. Using automatic source-detection software, we assemble a homogeneously-detected sample of 59 Ly $\alpha$  emitters covering a flux range of  $-18.0 < \log_{10}(F) < -16.3$  (erg s<sup>-1</sup>cm<sup>-2</sup>), corresponding to luminosities of  $41.4 < \log_{10}(L) < 42.8$  (erg s<sup>-1</sup>). As recent studies have shown, Ly $\alpha$  fluxes can be underestimated by a factor of two or more via traditional methods, and so we undertake a careful assessment of each object’s Ly $\alpha$  flux using a curve-of-growth analysis to account for extended emission. We describe our self-consistent method for determining the completeness of the sample, and present an estimate of the global Ly $\alpha$  luminosity function between redshifts  $2.91 < z < 6.64$  using the  $1/V_{max}$  estimator. We find the luminosity function is higher than many number densities reported in the literature by a factor of 2–3, although our result is consistent at the  $1\sigma$  level with most of these studies. Our observed luminosity function is also in good agreement with predictions from semi-analytic models, and shows no evidence for strong evolution between the high- and low-redshift halves of the data. We demonstrate that one’s approach to Ly $\alpha$  flux estimation does alter the observed luminosity function, and caution that accurate flux assessments will be crucial in measurements of the faint end slope. This is a pilot study for the Ly $\alpha$  luminosity function in the MUSE deep-fields, to be built on with data from the *Hubble Ultra Deep Field* which will increase the size of our sample by almost a factor of 10.

**Key words:** cosmology:observations - surveys - galaxies:evolution - galaxies:formation - galaxies:high-redshift - galaxies:luminosity functions.

## 1 INTRODUCTION

The Ly $\alpha$  emission line is one of the most powerful probes of the early Universe, giving us insight into the very early stages of galaxy formation. Galaxies detected via their Ly $\alpha$ -emission (LAEs; Cowie & Hu 1998) offer us a means to study high-redshift star-forming galaxies, even with continuum magnitudes too faint to be observed using current technology. These low-mass objects form the building blocks of  $L^*$  galaxies in the local Universe

(Dayal & Libeskind 2012, Garel et al. 2016), meanwhile theoretical models suggest they may also play a significant role in driving cosmic reionisation e.g. Gronke et al. (2015a), Dijkstra et al. (2016), Santos et al. (2016).

Although Ly $\alpha$  physics is complex (e.g. Verhamme et al. 2006, Gronke et al. 2015b), we can begin to understand the physical processes underway at these epochs by measuring the luminosity function of LAEs – a fundamental statistic of the population. The lu-

minosity function tells us about the relative abundance of different luminosity objects in the overall distribution (e.g. see Johnston 2011), and ultimately for deep enough samples, measurement of the faint-end slope will tell us if LAEs are numerous enough to be the primary sources of reionisation (see Dressler et al. 2015 for a discussion).

The largest samples of LAEs to date come from narrow-band selection, whereby a narrow filter (typically  $< 100 \text{ \AA}$ ), is used in combination with broad-band photometry to detect emission-line galaxies in distinct redshift “slices”. This approach is very efficient, having led to samples of thousands of  $H\alpha$ ,  $H\beta$ , [OIII] and [OII] emitters out to  $z \approx 2.0$  (Sobral et al. 2009, Sobral et al. 2013, Drake et al. 2013, Drake et al. 2015) as well as LAEs at  $z > 3.0$  (Rhoads et al. 2000, Ouchi et al. 2003, Hu et al. 2004, Ouchi et al. 2008, Yamada et al. 2012, Matthee et al. 2015, Konno et al. 2016, Santos et al. 2016). These relatively shallow surveys have provided increasingly robust estimates of the  $\text{Ly}\alpha$  luminosity function down to luminosities of  $\log_{10} L \approx 42.0 \text{ erg s}^{-1}$ , in the redshift interval  $\approx 2.0 < z < 7.0$ . Typically these studies estimate values of the characteristic number density and luminosity of the sample, although the faint-end slope remains unconstrained.

Spectroscopic studies provide an alternative approach, allowing the identification of LAEs without any need for ancillary data, but typically surveying far smaller volumes. In addition to targetted spectroscopy, one can place long-slit spectrographs blindly on sky, but the results often suffer from severe slit-losses and a complicated selection function. (See also survey results from low-resolution slitless spectroscopy Kurk et al. 2004, Deharveng et al. 2008 and IFU studies van Breukelen et al. 2005, Blanc et al. 2011). In recent years, spectroscopic surveys have begun to push  $\text{Ly}\alpha$  samples to lower flux limits than ever before, complementing wide, shallow, studies with very deep integrations. The two deepest such surveys to date come from Rauch et al. (2008) and Cassata et al. (2011) reaching 1 dex deeper than their narrow-band counterparts. Rauch et al. (2008) used a 92 hour long-slit exposure with the ESO VLT FORS2 instrument, detecting single-line emitters of just a few  $\times 10^{-18} \text{ erg s}^{-1} \text{ cm}^{-2}$  corresponding to  $\text{Ly}\alpha$  luminosities of  $\approx 8 \times 10^{40} \text{ erg s}^{-1}$  for LAEs in the range  $2.67 < z < 3.75$ . The authors note however that their luminosities could be underestimated by factors of 2–5 due to slit losses, and the identification of many of their single-line emitters is somewhat uncertain. Another notable study came from the VIMOS-VLT Deep Survey (VVDS; Cassata et al. 2011) finding 217 LAEs with secure spectroscopic redshifts between  $2.00 < z < 6.62$ , and fluxes reaching as low as  $F = 1.5 \times 10^{18} \text{ erg s}^{-1} \text{ cm}^{-2}$ . The detections came from a combination of targetted and serendipitous spectroscopy however, and again resulted in a complex selection function and slit losses. Nevertheless, the number of emitters in their sample allowed the authors to split the data into three redshift bins, to look for any sign of evolution in the observed luminosity function. They ultimately found no evidence in support of evolution, consistent with the previous results of van Breukelen et al. (2005), Shimasaku et al. (2006), and Ouchi et al. (2008). Finally, at the highest redshifts, the first robust constraints on the faint end of the  $\text{Ly}\alpha$  luminosity function came from Dressler et al. (2015). They found a very steep value of the faint-end slope at  $z = 5.7$ , using targets selected via “blind long-slit spectroscopy”, further reinforcing the significance of intrinsically faint LAEs in the early Universe (see also Dressler et al. 2011 and Henry et al. 2012).

The low-luminosity LAE population is now at the forefront of research, meaning that the accurate recovery of total LAE fluxes is of high priority for upcoming work. Indeed, some studies have

already suggested that all LAEs exhibit extended, low-surface-brightness  $\text{Ly}\alpha$  emission coming from the surrounding circumgalactic medium. The detection of this emission is difficult, and requires very sensitive measurements indeed. Momose et al. (2014) built on the work of Matsuda et al. (2012) by stacking LAE detections in 5 redshift slices between  $\approx 2.2 < z < 6.6$  resulting in the detection of extended  $\text{Ly}\alpha$  emission around normal star-forming galaxies across this entire epoch. They found typical exponential scale lengths of  $\approx 5 - 10 \text{ kpc}$ , but the emission was not detectable around any individual galaxy (see also Yuma et al. 2013 for individual detections of metal-line blobs at lower  $z$ ).

The Multi Unit Spectroscopic Explorer (MUSE; Bacon et al. 2010) on the Very Large Telescope (VLT) allows us to carry out blind spectroscopic selection of LAEs between redshifts  $\approx 3.0 < z < 6.5$  with a homogeneous selection function. The efficiency of this approach to detect line emission allows us to use MUSE as a detection machine for the kind of star-forming galaxies we wish to trace, also enabling an accurate assessment of total  $\text{Ly}\alpha$  fluxes. Bacon et al. (2015), hereafter B15, presented a blind-spectroscopic analysis of the *Hubble Deep Field South* (HDFS), and the resultant catalogue showcased the detection power of MUSE. Indeed, B15 presented several galaxies detected via their line emission alone, that were otherwise undetectable in the deep broad-band HST imaging ( $I_{814} > 29 \text{ mag AB}$ ). Additionally, MUSE is able to overcome the effects of slit-loss that have so far hampered  $\text{Ly}\alpha$  flux estimates from long-slit spectroscopy, allowing us to perform a careful evaluation of the total  $\text{Ly}\alpha$  flux from each galaxy. For instance, Wisotzki et al. (2016) used a curve-of-growth analysis on 26 isolated halos in the B15 catalogue, and presented the first ever detections of extended  $\text{Ly}\alpha$  emission around individual, high-redshift, star-forming galaxies. The objects presented were in the flux range  $4.5 \times 10^{-18} \text{ erg s}^{-1} \text{ cm}^{-2}$  up to  $3 \times 10^{-17} \text{ erg s}^{-1} \text{ cm}^{-2}$  across the redshift interval  $2.96 < z < 5.71$ , and halos were detected around 21 of these objects. The omission of this low surface brightness contribution to the total  $\text{Ly}\alpha$  flux has potentially led to a systematic underestimation of  $\text{Ly}\alpha$  fluxes in the literature, and lends support to the importance of a re-assessment of the  $\text{Ly}\alpha$  luminosity function.

In this paper we present a pilot study for the LAE luminosity function using blind spectroscopy in the 1 square arcminute HDFS field. We use automatic detection software to present a homogeneously selected sample of 59 LAEs and estimate  $\text{Ly}\alpha$  fluxes via a curve-of-growth analysis to account for extended  $\text{Ly}\alpha$  emission. We have developed and implemented a self-consistent method to determine the completeness of our sample, allowing us to compute a global  $\text{Ly}\alpha$  luminosity function using the  $1/V_{max}$  estimator.

The outline of this paper is as follows. In Section 2 we present our observations from MUSE and outline our method of catalogue construction and sample selection. In Section 3 we describe our approach to estimating the  $\text{Ly}\alpha$  flux, and in Section 4 we present and discuss our completeness estimates for the sample. In Section 5 we present our estimation of the LAE luminosity function between  $2.91 < z < 6.64$ , and discuss our results in the context of observational literature as well as in comparison to the semi-analytic model of Garel et al. (2015). In Section 6 we examine the effect of using different flux estimates for LAEs and look for evolution over the redshift range of our observed luminosity function. Finally, we summarise our results in Section 7.

The total co-moving volume between  $2.91 < z < 6.64$  equates to  $10351.6 \text{ Mpc}^3$ . As parts of the cube are excluded from the search however (see Section 2.2.1) the total co-moving survey volume is reduced to  $10144.57 \text{ Mpc}^3$ . Throughout this paper we as-

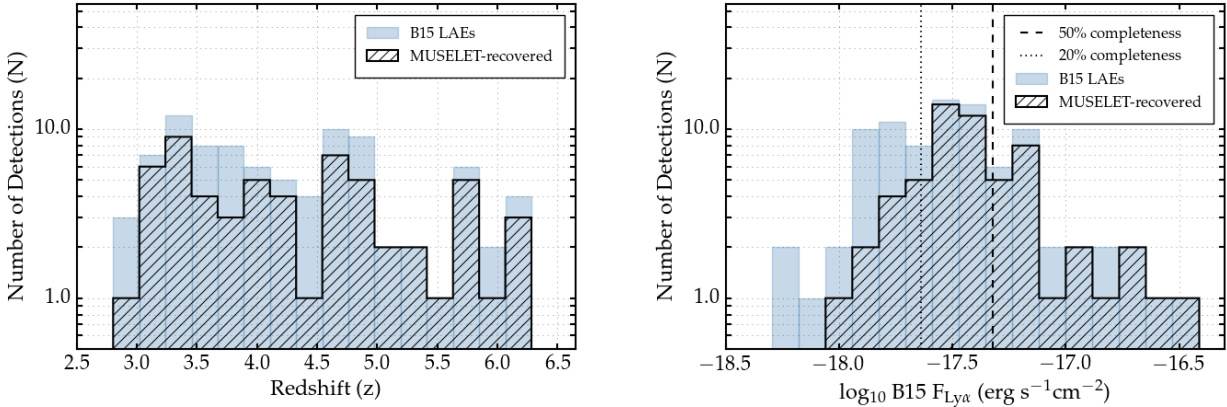


**Figure 1.** A comparison between numbers of LAEs presented in Bacon et al. (2015) and detections recovered using the detection software MUSELET. In the left-hand panel we show the redshift distribution of our detections overlaid on the redshift distribution of the B15 LAEs. This demonstrates an even recovery rate across the entire redshift range i.e. no redshift bias in our method of detection. In the right-hand panel we use the published flux estimates of B15 to show the distribution of fluxes recovered by MUSELET vs the distribution for B15 LAEs. We successfully recover the majority of bright LAEs before incompleteness becomes more apparent below  $\log_{10} F \text{ Ly}\alpha (\text{B15}) = -17.32$ . Bright LAEs which are not recovered by MUSELET lie in the small parts of the cube with fewer than 50 percent of the final exposure time. The average sample completeness is overlaid (dashed and dotted lines) and its derivation is described in Section 4.

sume a  $\Lambda$ CDM cosmology,  $H_0 = 70.0 \text{ km s}^{-1} \text{ Mpc}^{-1}$ ,  $\Omega_m = 0.3$ ,  $\Omega_\Lambda = 0.7$ .

## 2 DATA AND SAMPLE SELECTION

### 2.1 Observations and Data Reduction

During the final MUSE commissioning run in July 2014, we performed a deep integration on the HDFS for a total of 27 hours, using the standard wavelength range 4750-9300 Å. Seeing was good for most nights ranging between 0.5-0.9 arcsec. The full details of these observations are given in B15.

We use a new reduction of the cube optimised for the detection of faint emission-line objects (v1.4; Cantalupo, in prep). The reduction uses the CubExtractor package and tools to minimise residuals around bright sky lines. For a more detailed description of the flat-fielding and sky-subtraction procedures with the CubExtractor package see, e.g. Borisova et al. (2016). A detailed comparison between this improved reduction for the HDFS field with respect to previous versions will be presented in Cantalupo et al., in prep.

### 2.2 Catalogue Construction

When assessing the luminosity function, it is of fundamental importance to understand the selection function of the galaxies which make up the sample. This means that the catalogue of LAEs must be constructed homogeneously, and in a way which allows us to assess the completeness of the sample in a consistent manner.

We therefore choose to implement a single method of source detection allowing us to apply homogeneous selection criteria across the field, and to apply these same criteria in our fake source recovery experiment (see Section 4). We highlight here that any automated catalogue construction will require some trade-off to be made between the depth of the catalogue and the false detections which are included. In this work, we choose a conservative setup of our detection software to minimise false detections, resulting in a very robust selection of objects.

Finally, one needs to verify the nature of each source as an LAE, and for this we rely on the deeper catalogue presented in B15 (details below). This means that by construction, our catalogue will always form a subsample of B15. While the B15 catalogue is deep and meticulously constructed, the objects were detected through a variety of means, and the heterogeneity of the sample results in an irregular selection function which would be impossible to reproduce. For this reason the B15 catalogue is unsuitable for the construction of a luminosity function.

#### 2.2.1 Source Detection

Our chosen software, “MUSELET” (J. Richard), has been optimised for the detection of line emission, and has been extensively tested on both blank and cluster fields. MUSELET makes extensive use of the SEXTRACTOR package (Bertin & Arnouts 1996) to perform a systematic search through the data cube for emission-line objects. The input data cube is manipulated to create a continuum-subtracted narrow-band image at each wavelength plane. Each narrow band image is based on a line-weighted average of 5 wavelength planes in the cube (6.25 Å total width), and the continuum is estimated from 2 spectral medians of  $\approx 25 \text{ \AA}$  on each the blue and the red side of the narrow band region. SEXTRACTOR is run on each of these images as they are created<sup>1</sup>, using the exposure map cube as a weight map, and rejecting all detections in areas of the cube with fewer than 50 percent of the total number of exposures. This reduces the volume probed to 0.98 of the full cube, and is taken into account in the construction of the luminosity function. Once the entire cube has been processed, MUSELET merges all of the SEXTRACTOR catalogues, and records a detection at the wavelength of the peak of the line. This results in a “raw” catalogue of emission lines.

<sup>1</sup> SEXTRACTOR parameters are set to DETECT MINAREA = 3.0, and DETECT THRESH = 2.5. These are the minimum number of pixels above the threshold and the sigma of the detection respectively.

### 2.2.2 Candidate LAE Selection

MUSELET includes the option to interpret this raw catalogue of detections as individual objects. Using an input list of rest-frame emission line wavelengths and flux ratios, we can combine lines coincident on-sky, and estimate a best redshift for each object showing multiple emission peaks. Emission lines are merged spatially into the same source based on the “radius” parameter (here radius = 4 pixels or 0.8 arcseconds), and the object must be detected in two consecutive narrowband images in the cube to register as a real source.

Thanks to the wavelength coverage and sensitivity of MUSE, we anticipate the detection of multiple lines for galaxies exhibiting any of the major emission lines associated with star formation. Only those sources exhibiting a single emission line are flagged as “Ly $\alpha$ /[OII]” emitters for validation. This equates to 144 single-line sources.

### 2.2.3 LAE Verification

We now have a robustly detected catalogue of single line emitters, and we rely on the detailed work presented in B15 to give us a means to distinguish between Ly $\alpha$  and [OII] emitters. Of the 144 single line emitters detected with MUSELET, 59 are identified as LAEs through careful matching to B15. To qualify as a match to the B15 catalogue, the positions on sky must lie within a 1.0 arcsecond radius of one another and within 6.25 Å in wavelength. The B15 catalogue was constructed taking full advantage of the deep HST imaging across the field, initially extracting spectra at the positions of objects presented in the HST catalogue of Casertano et al. (2000). In a complementary approach, several pieces of detection software<sup>2</sup> were used to search for pure emission-line objects as liberally as possible, as well as several searches conducted by eye. Via each of these methods, all detections were scrutinised by at least two authors of B15, comparing spectral extractions, narrow-band images and HST data before the object was validated.

### 2.2.4 Final Catalogue

In the left-hand panel of Figure 1 we show the redshift distribution of the 89 B15 LAEs with secure identifications ( $Q \geq 2$ )<sup>3</sup> according to the assigned confidence level in B15. Overlaid is the distribution of the MUSELET-selected LAE sample which match to existing objects in B15. We find recovery is evenly distributed across the entire redshift range in the deeper B15 catalogue, indicating no redshift bias in our object detection. In the right-hand panel of Figure 1, we show the distribution of fluxes reported in B15 for the same two samples. Ly $\alpha$  flux values in B15 come from PLATEFIT (Tremonti et al. 2004) 1D spectral extraction estimates, using a Gaussian profile fit to the Ly $\alpha$  line. We note that this is not the optimal procedure to estimate Ly $\alpha$  flux, and we do not use these values in the determination of the luminosity function or the remainder of this paper - see Section 3 for a discussion of the factors affecting flux estimation and a description of our improved approach.

We recover almost all LAEs with a B15 flux greater

<sup>2</sup> SExtractor; Bertin & Arnouts (1996), LSDcat; Herenz et al. (in prep)

<sup>3</sup> Confidence levels in B15 range between  $Q=0$  (no secure redshift) and  $Q=3$  (redshift secure and based on multiple features).  $Q=2$  refers to a single-line redshift with a high signal to noise (i.e. to distinguish between the Ly $\alpha$  and [OII] line profiles).

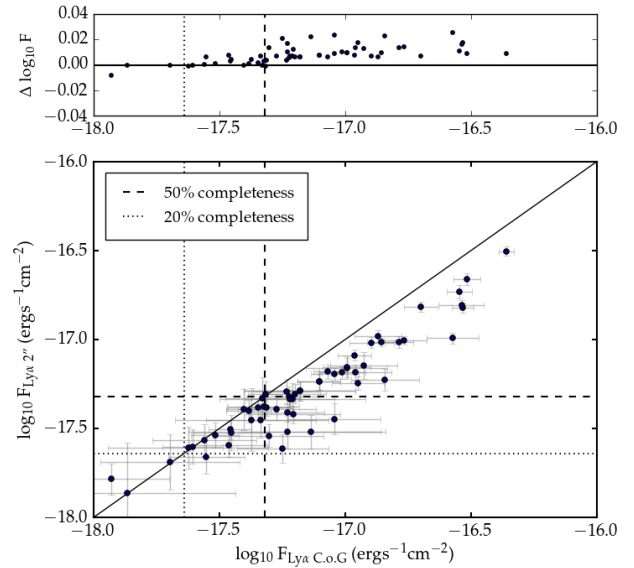


**Figure 2.** Comparison of Ly $\alpha$  flux estimates. The upper panel shows  $\Delta \log_{10} F$  as a function of  $F_{C.o.G.}$ , where  $\Delta \log_{10} F = (\log_{10} F_{2''} - \log_{10} F_{C.o.G.}) / \log_{10} F_{C.o.G.}$ . The lower panel shows a direct comparison of flux estimates from  $F_{2''}$  and  $F_{C.o.G.}$ . Error bars depict the standard deviation from pixel statistics on each flux measurement. The sample completeness (overplotted dashed and dotted lines) is described in Section 4. While the two estimates agree at fluxes lower than  $\log_{10} F \approx -17.3$ , brighter than this the two measurements deviate increasingly, highlighting the need for a careful assessment of total flux when dealing with LAEs.

than the average 50 percent sample completeness limit at  $\log_{10} B15 F_{Ly\alpha} = -17.32$  (see Section 4). We miss only those that lie in parts of the cube with fewer than 50 percent of the total exposure time which are rejected by MUSELET, but seen by eye or alternative software in B15. We detect 24 of the 26 bright isolated LAEs presented in Wisotzki et al. (2016) which were drawn from the B15 sample. On visual inspection these two objects, although bright, are found in the very small parts of the cube with less than 50 percent of the total exposure time, and therefore are not recovered with the chosen MUSELET setup.

For the remainder of the analysis, we make the assumption that any MUSELET single line detections which are not verified as LAEs by the extensive B15 catalogue are [OII] emitters or spurious detections, and can be excluded from the analysis.

## 3 FLUXES

The accurate recovery of line fluxes plays an important role in determining the luminosity function. In addition to the difficulties of flux measurement from long-slit spectroscopic observations, B15 noted that even when utilising a data cube, in deep integrations such as these, source crowding can lead to necessarily small spectral extractions, and hence the outer parts of extended sources can be unaccounted for. In the case of the fluxes quoted in B15, the flux underestimate will be exacerbated in some cases due to the fact that

PLATEFIT was not designed to deal with LAEs which often exhibit an asymmetric profile. Wisotzki et al. (2016) reported for instance that Ly $\alpha$  fluxes in B15 from PLATEFIT were sometimes more than a factor of two too low.

Our preferred approach is to perform photometry on pseudo narrow-band images constructed by collapsing several planes of a datacube in the spectral direction allowing us to treat the outer parts of each source with greater care. We conduct this analysis in two ways in order to demonstrate the difference in measured LAE fluxes when working with different sized apertures to those which have often been used in the literature.

### 3.1 Methods of Ly $\alpha$ Flux Estimation

For each confirmed LAE, we extract a 1D spectrum from the cube, using an aperture defined by the segmentation map from SExtractor. This spectrum is used only to gain some measure the FWHM of the line, by fitting a Gaussian to the profile. Next we extract a “narrow-band” image from the cube centred on the detection wavelength, of width  $\Delta\lambda = 4 \times \text{FWHM}$ , and a “continuum image” on the red side of the line, offset by  $50 \text{ \AA}$ , and of width  $\Delta\lambda = 200 \text{ \AA}$ . Finally, we subtract the mean continuum image from the mean narrow-band image to construct a “Ly $\alpha$  image” (multiplied by the width of the narrowband image for correct flux units). We perform all photometry on this final image, masking objects in close proximity to the LAE, seen in the corresponding continuum or narrow-band images.

We consider two different approaches to flux estimation using aperture photometry on the Ly $\alpha$  images. First we conduct photometry in an aperture of 2 arcseconds in diameter, and then carry out a curve-of-growth analysis using the light profile of each object to judge the appropriate size of aperture to account for extended emission. To measure the light profile of each object, we centre an annulus on the object in our masked Ly $\alpha$  image, before stepping through consecutive annuli of increasing radii measuring the flux in each ring. The total flux is then determined as the sum of the annuli out to the radius where the mean flux in an annulus reaches or drops below zero. This is where the light profile of the object hits the background of the image. Removing the local background of the objects made no significant impact on our results.

### 3.2 Comparison of Flux Estimates

Figure 2 shows a comparison between the measured two arcsecond aperture flux,  $F_{2''}$ , and the curve of growth flux,  $F_{C.o.G.}$ . The estimates are in good agreement below  $F \approx -17.3$  which is also where the sample reaches an average completeness of 50 percent (see Section 4 for details). Upwards of this,  $F_{C.o.G.}$  starts to deviate more dramatically from  $F_{2''}$ . This means that flux measurements of the brightest LAEs will differ most according to the approach used, possibly introducing some bias into measurements of the luminosity function at different redshifts. We investigate the effect of different methods of flux estimation on the luminosity function in Section 6.1.

The objects blindly detected by MUSELET are summarised in Table A1 with Ly $\alpha$  flux estimates resulting from our curve of growth analysis as well as two arcsecond aperture photometry. Errors on our flux estimates are given by the standard deviation of each measurement according to pixel statistics. We also show the published Ly $\alpha$  fluxes from both B15 and Wisotzki et al. (2016) where 26 objects were carefully re-examined.

## 4 SAMPLE COMPLETENESS

### 4.1 Fake Source Recovery

To make quantitative measures of the completeness of our LAE sample from MUSELET, we insert fake point-source line emitters distributed randomly on-sky into the real data cube. For each fake line-emitter the properties of the Ly $\alpha$  line profile (asymmetry and velocity width) are drawn randomly from the measured profiles of the LAEs presented in B15, and the objects are required to scatter randomly on-sky with no avoidance of each other or of real objects. By definition this means that the completeness estimate will never reach 100 percent as objects can fall on top of one another, behind real sources, or in the small volume of the cube where exposure time is less than 50 percent of the total integration where sources are rejected by MUSELET. This allows an exact imitation of the method via which we construct our catalogue, and ensures that the two volumes surveyed are identical.

We work systematically through the data cube inserting 20 fake LAEs at a time in redshift bins of  $\Delta z = 0.01$  corresponding to wavelength intervals of  $\approx 12 \text{ \AA}$ . Each point-source LAE is convolved with the MUSE PSF to create a tiny cube containing only an LAE spectrum (no continuum emission) and its associated shot noise in a variance cube. The mini data- and variance cubes are then added directly to the real data and variance cubes. Crucially, we make the assumption here that all input fake LAEs would indeed be correctly classified by matching to B15.

### 4.2 Completeness as a Function of Luminosity

In Figure 3 we show the recovery fraction of LAEs with MUSELET as a function of log luminosity. We use 40 values of log luminosity, and 370 tiny redshift bins, showing LAE-redshift in the colour bar.

In the lowest redshift bin at  $z = 3.00$ , we begin to detect objects at  $\log_{10}(L) \approx 40.65$ , reaching a 90 percent recovery rate by  $\log_{10}(L) \approx 41.20$ . By redshift  $z = 6.64$  objects are not recovered unless their luminosity exceeds  $\log_{10}(L) = 41.65$ , reaching 90 percent completeness by  $\log_{10}(L) = 42.60$ . In addition to the shift towards brighter luminosities for each completeness curve with increasing redshift, the gradient of each curve also gradually decreases with increasing redshift. This behaviour is due to night sky emission becoming more prominent towards longer wavelengths, and hampering the detection of even luminous LAEs at higher redshifts. Taking the lowest and highest redshift bins again, we see that the recovery fraction in the lowest redshift bin goes from 10 to 90 percent across a luminosity interval of 0.40 dex, whereas at the highest redshifts in the sample, the same interval in completeness spans a luminosity range of 0.75 dex. This reinforces our choice of a very finely sampled redshift range, as completeness levels will vary significantly according to the proximity of each LAE’s observed wavelength to sky lines.

In order to approximate the average completeness of the sample in terms of LAE flux, we can combine these results across all wavelengths. Using the input redshift and luminosity of each fake LAE, we can determine its flux, and record the information of whether the object was recovered by MUSELET or not. This way we estimate that the sample completeness drops to 50 percent by  $\log_{10}(F) = -17.32$  and 20 percent by  $\log_{10}(F) = -17.64$ . Completeness levels as a function of flux will depend strongly on observed wavelength, and hold only for a particular setup of detection software. We therefore only present these limits as the “average sample completeness”, to give a rough indication of the depth of the LAE sample (particularly in Figure 1, RHS, and Figure 2).

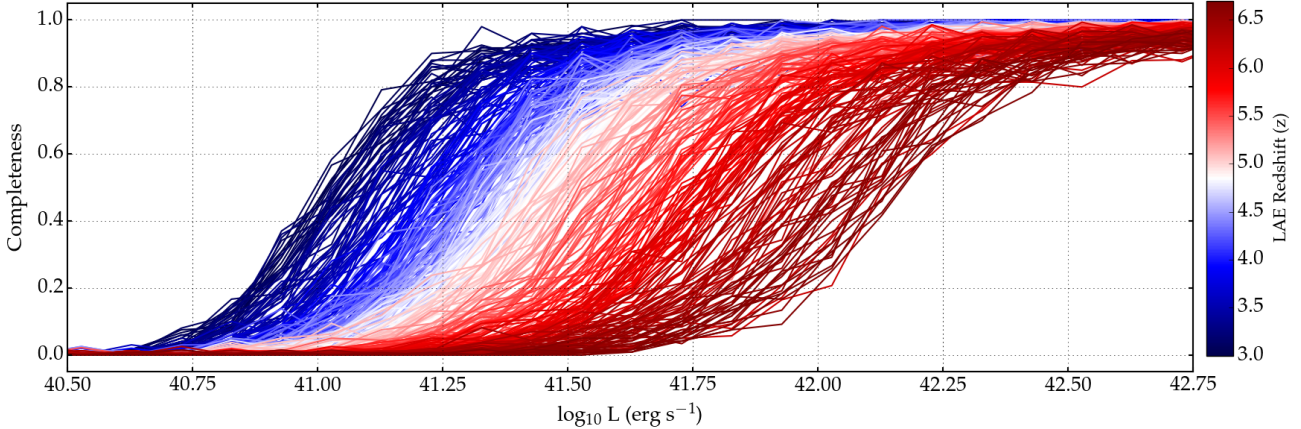


**Figure 3.** Completeness as a function of LAE luminosity. We show the recovery fraction of LAEs at 40 different input luminosities, colour-coded by redshift in intervals of  $\Delta z = 0.01$  ( $\Delta\lambda \approx 12 \text{ \AA}$ ). At higher redshifts LAEs must have a higher luminosity before they can be detected. Additionally, the detectability of higher redshift LAEs increases more slowly with increasing luminosity since night sky emission hampers observations towards longer wavelengths.

## 5 RESULTS

### 5.1 Luminosity Functions

Using the 59 objects presented here, we implement the  $1/V_{\max}$  estimator to assess the global luminosity function for LAEs in the redshift range  $2.91 < z < 6.64$ . The results are presented in Table 1 and Figure 4.

For each LAE,  $i$ , in the catalogue, the redshift  $z_i$  is determined according to  $z_i = \lambda_i/1215.67 - 1.0$ , where  $\lambda_i$  is the observed wavelength of Ly $\alpha$  according to the peak of the emission detected by MUSELET. The luminosity  $L_i$  is then computed according to  $L_i = f_i 4\pi D_L^2(z_i)$ , where  $f_i$  is the Ly $\alpha$  flux measured in our curve of growth analysis,  $D_L$  is the luminosity distance, and  $z_i$  is the Ly $\alpha$  redshift. The maximum co-moving volume within which this object could be observed,  $V_{\max}(L_i, z_i)$ , is then computed by:

$$V_{\max}(L_i, z_i) = \int_{z_1}^{z_2} \frac{dV}{dz} C(L_i, z_i) dz \quad (1)$$

where  $z_1 = 2.91$  and  $z_2 = 6.64$ , the minimum and maximum redshifts of the survey respectively,  $dV$  is the co-moving volume element corresponding to redshift interval  $dz = 0.01$ , and  $C(L_i, z_i)$  is the completeness curve for an object of luminosity  $L_i$ , across all redshifts  $z_i$ .

The number density of objects per luminosity bin,  $\phi$ , is then calculated according to:

$$\phi[(\text{dlog}_{10}L)^{-1} \text{Mpc}^{-3}] = \sum_i \frac{1}{V_{\max}(L_i, z_i)} / \text{binsize} \quad (2)$$

where in this instance the bin size is 0.35 dex.

Figure 4 shows the differential Ly $\alpha$  luminosity function across the redshift range  $2.91 < z < 6.64$ , using a curve-of-growth analysis of the Ly $\alpha$  flux. In the upper panel we show the values of  $\phi$  given by the  $1/V_{\max}$  estimator, and in the lower panel a histogram depicts the numbers of objects found in each bin. Overlaid on the

lower panels are the completeness curves as a function of luminosity at three example redshifts ( $z = 3.00, 4.78$  and  $6.64$ ) to give an indication of the range of completeness corrections being applied to objects in each bin. Notably in the lowest luminosity bins completeness corrections can range from 0 to over 90 percent, and so small inaccuracies in the completeness estimate will potentially result in significant changes to the luminosity function here.

In our central luminosity range where the bins are most well-populated, our data are a factor of 2–3 higher than many of the results from previous studies, although the  $1\sigma$  Poissonian error on our points touches a couple of the literature results, or failing this the error bars overlap. Additionally, although our highest luminosity bin (containing only a single object) is in perfect agreement with the well-constrained literature at this luminosity, we note that the bin is incomplete, and correcting for this would likely place the data point above the literature again.

### 5.2 Comparison to Literature

In the following paragraphs we make a more detailed comparison to literature results from the various commonly-adopted approaches to LAE selection: narrow-band studies, blind long-slit spectroscopy, early IFU data, and lensed LAEs detected with MUSE (Bina et al. 2016)<sup>4</sup>. We note that these studies themselves are dispersed due to cosmic variance, slit-losses, small apertures and different equivalent width limits.

In comparison to the narrow-band studies shown, our data sit higher at all luminosities than Ouchi et al. (2008) at  $z = 3.00$  and  $z = 3.70$ , but always within the error bars of the narrowband data. We are in agreement across all datapoints with Ouchi et al. (2008) at  $z = 5.00$ , however this study does have larger error bars than their lower redshift data. The final two narrowband studies are Dawson

<sup>4</sup> Note that the points we show here from Abell 1689 are an updated version of Bina et al. (2016) correcting for an error in the survey volume that they originally calculated.

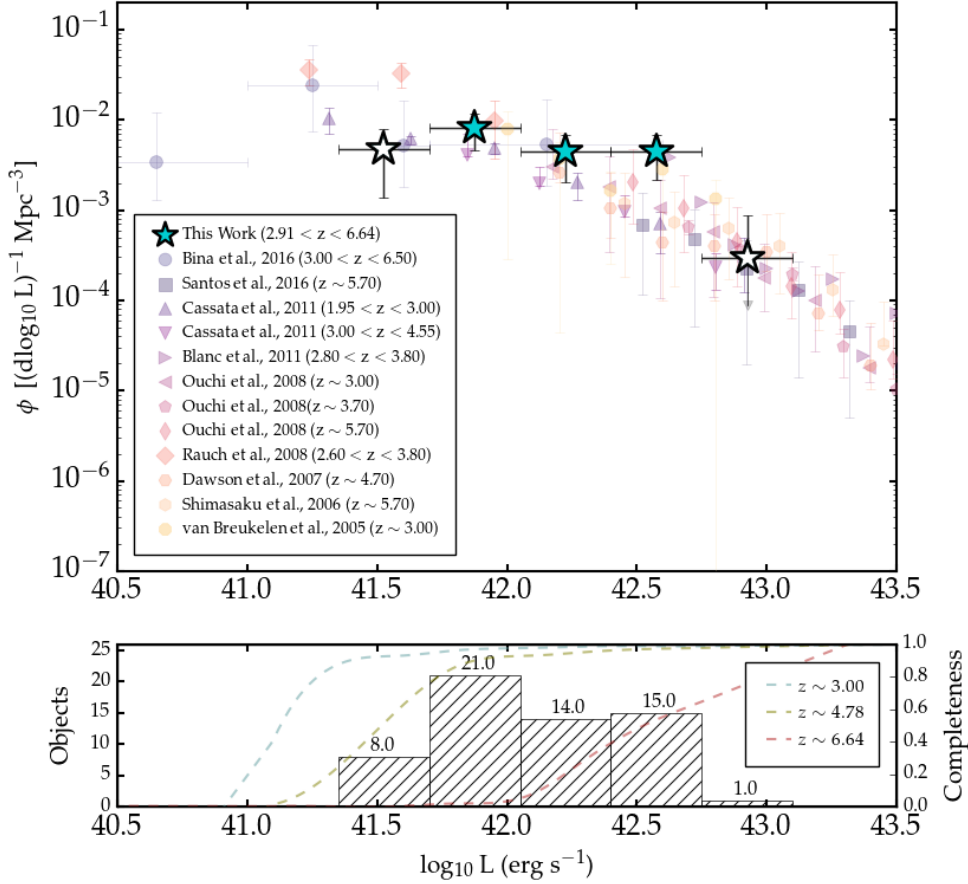


**Figure 4.** In the upper panel we show the Ly $\alpha$  luminosity function estimated across the entire redshift range  $2.91 < z < 6.64$  in the context of other surveys in the literature. We use Ly $\alpha$  fluxes estimated using a curve-of-growth analysis and calculate values of  $\phi$  using the  $1/V_{max}$  estimator. Our faintest and brightest bins are marked with a transparent star to signify that the bins are incomplete and should be interpreted with caution. The literature data come from narrow-band surveys (Ouchi et al. 2008: left-pointing triangle at  $z \approx 3.00$ , pentagon at  $z \approx 3.70$ , narrow diamond at  $z \approx 5.70$ , Dawson et al. 2007: hexagon at  $z \approx 4.70$ , Santos et al. 2016: square at  $z \approx 5.70$ ), blind or targeted long-slit spectroscopy (Rauch et al. 2008: wide diamond at  $2.60 < z < 3.80$ , Cassata et al. 2011: upwards-pointing triangle at  $1.95 < z < 3.00$ , downwards-pointing triangle at  $3.00 < z < 4.55$ , Shimasaku et al. 2006 at  $z \approx 5.70$ ), and IFU studies (van Breukelen et al. 2005; octagons at  $z \approx 3.00$  and Blanc et al. 2011; right-pointing triangle at  $2.80 < z < 3.80$ , Bina et al. 2016; circles at  $3.00 < z < 6.50$ ). In the lower panel we show the associated histogram of luminosities, overlaid with completeness curves at three example redshifts. Our estimate of the luminosity function sits higher than many literature results in our most well-constrained bins, although within the  $1\sigma$  Poissonian errorbars.

**Table 1.** Differential Ly $\alpha$  luminosity function in bins of  $\Delta \log_{10} L = 0.35$ , including numbers of objects in each bin.

Bin $\log_{10}(L)$ [erg s $^{-1}$ ]	$\log_{10} L_{median}$ [erg s $^{-1}$ ]	$\phi$ [(dlog $_{10} L)^{-1}$ Mpc $^{-3}$ ]	No.
41.35 < <b>41.525</b> < 41.70	41.596	$0.0046 \pm 0.0033$	8
41.70 < <b>41.875</b> < 42.05	41.872	$0.0082 \pm 0.0036$	21
42.05 < <b>42.225</b> < 42.40	42.247	$0.0044 \pm 0.0024$	14
42.40 < <b>42.575</b> < 42.75	42.508	$0.0044 \pm 0.0023$	15
42.75 < <b>42.925</b> < 43.10	42.829	$0.0002 \pm 0.0005$	1

et al. (2007) and Santos et al. (2016) at  $z = 4.70$  and  $z = 5.70$  respectively, and fully consistent with one another. The Dawson et al. (2007) data reach  $\log_{10}(L) = 42.0$  and are in good agreement with our points except for our bin at  $\log_{10}(L) = 42.6$  where our value of  $\phi$  is significantly higher. The Santos et al. (2016) data are similar,

they reach down to slightly brighter than  $\log_{10}(L) = 42.5$ , and the only point in disagreement with our own is again our measurement at  $\log_{10}(L) = 42.6$  where we are significantly higher.

Our data point at  $\log_{10}(L) = 42.6$  sits almost exactly on top of two other data points, coming from the two other IFU studies

we examine (van Breukelen et al. 2005, Blanc et al. 2011). For Blanc et al. (2011) this is the faintest datapoint in their sample, but van Breukelen et al. (2005) reach almost 1 dex deeper where the data points agree with our data and are more in line with the rest of the literature as well. The error bars of the three IFU data points overlap with those of all three datasets from Ouchi et al. (2008), but it is interesting to note that all three studies are high in the  $\log_{10}(L) = 42.6$  bin, and inconsistent with both Dawson et al. (2007) and Santos et al. (2016).

Our faintest two bins at  $\log_{10}(L) = 41.75$  and  $\log_{10}(L) = 41.5$  can only be compared to the deep blind long-slit spectroscopy of Cassata et al. (2011) and Rauch et al. (2008), and the MUSE results from the lensing cluster Abell 1689 (Bina et al. 2016). Our  $\log_{10}(L) = 41.75$  datapoint sits between the brightest point from Rauch et al. (2008) and the faintest point from Cassata et al. (2011) at redshift  $3.00 < z < 4.55$ . Our value of  $\phi$  is consistent with both these points. Our lowest luminosity point lies below Cassata et al. (2011) at  $1.95 < z < 3.00$  although consistent with their result within errors, however the point lies significantly below the measurement of Rauch et al. (2008). Since this point is our lowest luminosity point, and is likely to suffer the most from small inaccuracies in completeness estimates, we do not interpret this point as having ruled out the result of Rauch et al. (2008), although the data are noticeably in better agreement with the values of Cassata et al. (2011). Finally, we compare to the results of Bina et al. (2016) who calculated the number density of LAEs behind lensing cluster Abell 1689. The 17 LAE luminosities range between  $40.5 < \log_{10}L < 42.5$  erg s<sup>-1</sup>, i.e. the deepest LAE data to date, and despite having applied no completeness correction, the values are broadly consistent with our own estimates. The errors on the small number of objects in Bina et al. (2016) mean that their values of  $\phi$  are entirely consistent with Cassata et al. (2011), as well as close to consistent with the Rauch et al. (2008) data points.

### 5.3 Cumulative Luminosity Function

In Figure 5 we show the cumulative Ly $\alpha$  luminosity function between redshifts  $2.91 < z < 6.64$ . Note that we show this Figure in a “zoomed-in” panel due to the data covering only a small part of the dynamic range of the literature shown in Figure 4. The cumulative luminosity function has the advantage of being sensitive to each individual object in the sample, alleviating the problem of lost information in a binned differential luminosity function, especially for small samples. Each object in the sample is visible in the function as a vertical step at the luminosity of the object. This allows us to visualise the distribution of objects within each bin of the differential luminosity function in Figure 4, for instance our lowest luminosity bin contains two objects towards the lower limit but is by no means an even distribution of luminosities. Equally, our highest luminosity bin contains only a single object lying towards lower luminosity edge. This allows us to interpret the density estimates in these bins with the appropriate level of caution.

### 5.4 Comparison to Models

In Figure 6 we compare our results to predictions from the mock lightcones used in Garel et al. (2016). The lightcones are generated using the model presented in Garel et al. 2015 (see Garel et al. 2012 for details) whereby the GALICS hybrid model of galaxy formation (Hatton et al. 2003) is coupled with numerical simulations of Ly $\alpha$  radiative transfer. GALICS combines an N-body cosmological simulation to follow the hierarchical growth of dark matter structures in

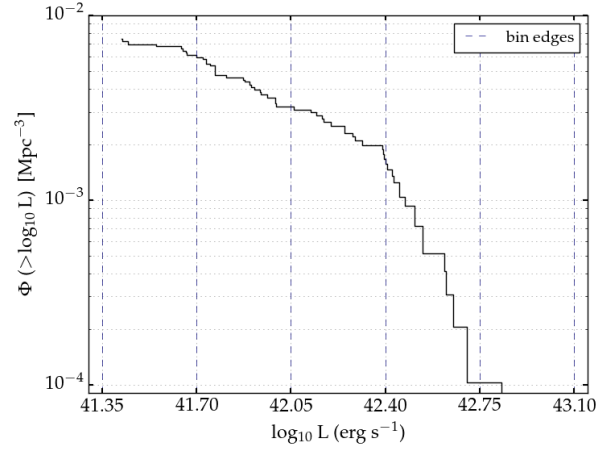


**Figure 5.** The cumulative Ly $\alpha$  luminosity function estimated across the entire redshift range  $2.91 < z < 6.64$ . Note that for clarity we zoom-in on the range of the data (this figure only). The step function gives an indication of how objects’ luminosities are distributed within each bin of the luminosity function in Figure 4, and allows us to interpret each bin with the appropriate level of caution.

a representative co-moving volume of  $(100 h^{-1} \text{ Mpc})^3$  with a semi-analytic component to describe the evolution of baryons within virialised dark matter halos. The escape of Ly $\alpha$  photons occurs through galactic outflows modelled as thin expanding shells of gas and dust (Schaerer et al. 2011, Verhamme et al. 2006). The escape fraction of each galaxy in Garel et al. (2015) is then determined by interpolating the shell parameters (expansion speed, HI column density, dust opacity and velocity dispersion) predicted by GALICS onto the grid of radiative transfer models of Schaefer et al. (2011).

We show the mean luminosity function over 1000 realisations of mock lightcones computed with the model of Garel et al. (2015). The geometry of the lightcones is adapted to mimic our survey of the HDFs (i.e.  $2.91 < z < 6.64$  over 1 square arcminute) and error bars give the  $1\sigma$  standard deviation of the measurement. Our data are in good agreement with the model, lying directly on top of the predicted number densities in the  $\log_{10}(L) = 41.88$  and  $\log_{10}(L) = 42.23$  bins as well as the single object in our  $\log_{10}(L) = 42.93$  bin. Our measurement in the  $\log_{10}(L) = 42.58$  bin once again sits high by a factor of  $\approx 3$ , with a  $1\sigma$  error bar just touching the  $1\sigma$  error on the model predictions. Finally, our lowest luminosity point at  $\log_{10}(L) = 41.53$  falls well below the model predictions from Garel et al. (2015), which is not surprising given the incomplete sampling of the bin. In the model, low-SFR galaxies have a higher Ly $\alpha$  escape fraction due to lower gas and dust contents such that the luminosity function continues to rise steeply towards faint luminosities ( $< 10^{42}$  erg s<sup>-1</sup>). This again emphasises the need for a more sophisticated completeness assessment for our sample to derive a more robust estimate of the luminosity function at the faint end, and thus better constrain LAE models.

Additionally, Garel et al. (2016) showed that the uncertainty on number counts in surveys of this volume will be dominated by cosmic variance, defined as the uncertainty in excess to that predicted by Poisson shot noise. This adds further motivation to our 9 by 9 square arcminute observations of the HUDF field with MUSE. In this forthcoming study, cosmic variance will be substantially re-

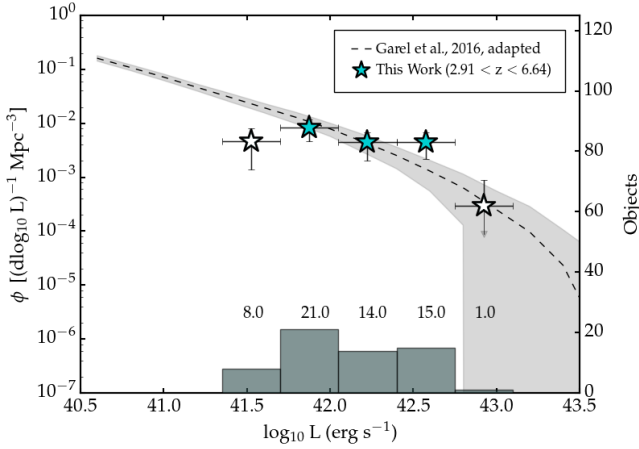


**Figure 6.** Comparison of our differential luminosity function to predictions from the semi-analytic model of Garel et al. 2015 (similar to those shown in Garel et al. 2016 but adapted to our survey volume). The error on the model prediction is the standard deviation from 1000 realisations of the mock lightcones produced by the model of Garel et al. (2015). The major component of this scatter comes from relative cosmic variance defined as the scatter in excess of that predicted by Poisson shot noise.

duced, but our data will still be deep enough to probe well below the knee of the luminosity function.

## 6 DISCUSSION

### 6.1 Luminosity Functions from Different Flux Estimates

In Section 3 we highlighted the difficulties of flux estimation from long-slit spectroscopy, in addition to the problems that arise from small aperture photometry. Figure 2 demonstrates how an aperture of diameter 2 arcseconds misses a great deal of flux for LAEs, which are known to exhibit extended emission. Here, in Figure 7, we examine the effect that each of these approaches to the flux measurement has on our resultant luminosity function. The luminosity function from  $F_{C.o.G}$  (shown in the large light blue circles) is the same that we show in Figure 4, and the luminosity function from  $F_{2''}$  is shown on the same axes in smaller dark blue circles. Changing the method of flux estimation means that objects jump between bins giving a different impression of the luminosity range under study. In the brightest overlap bin at  $\log_{10}(L) = 42.57$ , the value of  $\phi(F_{C.o.G})$  is significantly above  $\phi(F_{2''})$  as the measured flux of many objects has increased. In the faintest overlap bin however the opposite effect is seen, since some objects have shifted out of the bin towards higher measured luminosities. Notably the value of  $\phi(F_{2''})$  in this bin is in very good agreement with the value found in most literature studies. Realistic flux estimates will be of even greater importance when it comes to assessing the faint end slope, and so we re-assert their importance here.

### 6.2 Test for Evolution

Many studies have looked for signs of redshift-evolution in the observed Ly $\alpha$  luminosity function. van Breukelen et al. (2005), Shimasaku et al. (2006), Ouchi et al. (2008) and Cassata et al. (2011) all concluded that there was no evidence of such evolution in their

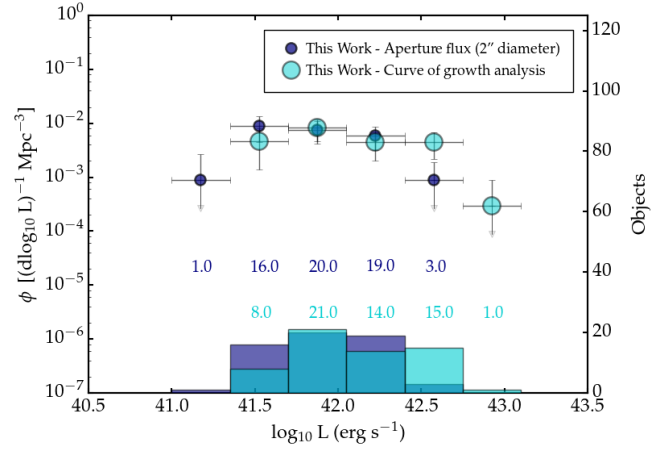


**Figure 7.** Luminosity functions from two different methods of estimating the total LAE flux. The small dark blue circles give values of  $\phi$  for photometry from a 2-arcsecond diameter aperture, and large light blue circles show values of  $\phi$  from a curve of growth analysis of total LAE flux. Due to objects shifting between bins the central measurements are in agreement, but the two approaches give different impressions of the luminosity range being studied, and will make a significant difference to measurements of the faint-end slope.

data. Here, with our small sample of objects, we can only make a crude attempt to look for evolution between  $z = 6.64$  and  $z = 2.91$ . We split the sample into high- and low-redshift subsets at the centre of the LAE redshift range and compare the two halves of the data, the number densities of objects in the two subsets can be seen in Figure 8. We see very little difference between the two halves, and indeed in each of the luminosity bins populated by both samples, the values of  $\phi$  are within the error bars of one another. As an additional check, we use a two-sample Kolmogorov-Smirnov test on the two distributions of volume-corrected luminosities (i.e. the values of  $1/V_{max}$ ) and find a two-tailed p-value of  $p = 3.345 \times 10^{-9}$  meaning we cannot discount the null hypothesis that the two distributions were drawn from the same underlying population. We conclude that there is no evidence of strong evolution between the two halves of the data – consistent with literature results – but note that we are limited by the small numbers of objects here, and a re-examination of the question is warranted with a richer dataset (Drake et al., in prep).

### 6.3 Limitations of our Study

Clearly our interpretation of the luminosity function is restricted by the small number of objects presented here, and the limitations of the  $1/V_{max}$  estimator. Although the faint-end of our luminosity function is broadly consistent with previous studies, our sample is not rich enough to constrain the steepness of the slope. In Drake et al., (in prep) we will dramatically increase the size of our dataset using LAEs in the *Hubble Ultra Deep Field* (HUDF) including several hundred sources from the MUSE HUDF  $9 \times 9$  square arcminute “mosaic” field. As discussed in Section 5.4, Garel et al. (2016) demonstrated that a study of this size and depth is the ideal survey design to examine the bulk of LAEs, while minimising the contribution of cosmic variance. In two complementary studies, the MUSE-WIDE program will substantially beat down statistics at

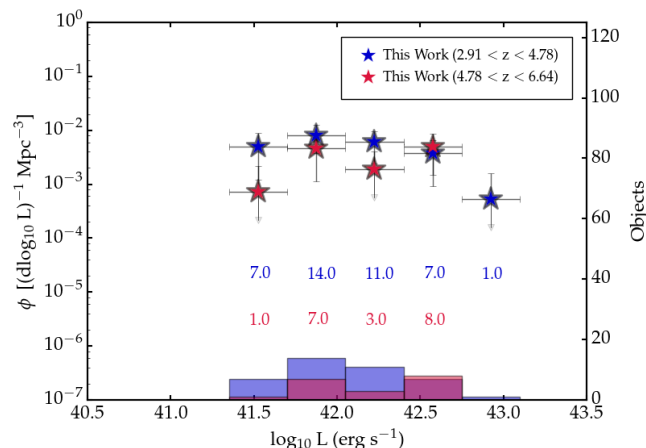


**Figure 8.** Luminosity functions derived for the high and low redshift halves of the dataset when split at the central LAE redshift detectable with MUSE. Blue stars show the low redshift half of the data, and red stars show the high redshift half of the data. At the bottom of the panel we show histograms of the luminosity distributions of the two halves of the dataset. The two distributions lie within the errorbars of one another, giving no evidence to suggest any redshift evolution in the observed luminosity function.

the bright-end of the luminosity function (Herenz et al., in prep), and MUSE GTO lensing fields will provide more of the deepest samples of LAEs to date. The combination of the MUSE-WIDE, MUSE-DEEP and MUSE-lensing fields will allow constraints on both the bright- and faint-end of the luminosity function, resulting in the most accurate measurement of the faint-end slope to date.

## 7 CONCLUSIONS

In summary, we have presented a homogeneous, automatically-detected sample of 59 LAEs in the HDFS using blind spectroscopy from MUSE. We validate the Ly $\alpha$  line through a careful matching to the deeper (heterogeneously constructed) catalogue of B15. We have shown that the method of Ly $\alpha$  flux estimation can significantly alter measured Ly $\alpha$  fluxes and investigated the effect this has on the luminosity function. We have designed a procedure self-consistent with our detection software to determine our selection function through recovery of fake point-source line emitters from deep MUSE datacubes, and compute a global Ly $\alpha$  luminosity function using a curve-of-growth analysis of the Ly $\alpha$  flux, and implementing the  $1/V_{max}$  estimator. We compare our results to literature studies, and semi-analytic model predictions from Garel et al. (2015), before finally examining the dataset for signs of evolution in the observed luminosity function.

Our main conclusions can be broadly summarised as follows:

- We automatically detect 59 LAEs in the HDFS across a flux range of  $\approx -18.0 < \log F < -16.3$  (ergs<sup>-1</sup>cm<sup>-2</sup>) using homogeneous and robust selection criteria, validating each LAE by matching to the deep catalogue of B15.
- Our global luminosity function between  $2.91 < z < 6.64$  sits higher by a factor of 2 – 3 than the literature in our most well-

constrained bins, although  $1\sigma$  errorbars overlap with the data of several literature studies at the same luminosity.

- The small drop in number density between our penultimate and faintest luminosity bin is likely to be entirely due to the limitations of our method; namely the effect of incomplete bins on the  $1/V_{max}$  estimator, and our idealised completeness assessment where LAEs are treated as point sources. We will investigate this in Drake et al., (in prep) using the MUSE HUDF mosaic sample.
- Our luminosity function is in good agreement with the semi-analytical model of Garel et al. (2015) with the exception of our bin at  $\log_{10} L = 42.58$ . The bin is once again a factor  $\approx 3$  higher than the predictions, with a  $1\sigma$  Poissonian error bar that just touches the  $1\sigma$  error on the model predictions.
- Method of Ly $\alpha$  flux estimation plays a role in the determination of the Ly $\alpha$  luminosity function and becomes most significant when measuring the faint end slope. Care should be taken here as studies start to probe further into the low-luminosity LAE population.
- When splitting our data at the central redshift and comparing the two halves of the data we see no evidence for strong evolution in the observed Ly $\alpha$  luminosity function across the redshift range  $2.91 < z < 6.64$ . This is entirely consistent with results in the literature.

Our pilot study demonstrates the efficiency of MUSE as a detection machine for emission-line galaxies, and strongly motivates our analysis of the HUDF  $9 \times 9$  square arcminute mosaic. The conservative nature of our selection process means that the objects presented here represent a robustly-selected sub-sample of the galaxies MUSE will ultimately detect and identify, and this is very encouraging for the potential of additional blank-field datasets from MUSE.

## ACKNOWLEDGEMENTS

This work has been carried out thanks to the support of the ANR FOGHAR (ANR-13-BS05-0010-02), the OCEVU Labex (ANR-11-LABX-0060) and the A\*MIDEX project (ANR-11-IDEX-0001-02) funded by the “Investissements d’avenir” French government program managed by the ANR. ABD thanks CRAL and ANR FOGHAR (ANR-13-BS05-0010-02), the Astrophysics Research Institute, Liverpool John Moores University, UK, for supporting a visiting fellowship, and Phil James for proof-reading. We make extensive use of the Muse Python Data Analysis Framework software (MPDAF), thanks to L.Piqueras. JR acknowledges support from the ERC starting grant 336736-CALENDS. TG is grateful to the LABEX Lyon Institute of Origins (ANR-10-LABX-0066) of the Université de Lyon for its financial support within the programme ‘Investissements d’Avenir’ (ANR-11-IDEX-0007) of the French government operated by the National Research Agency (ANR). LW and ECH acknowledge support by the Competitive Fund of the Leibniz Association through grant SAW-2015-AIP-2. JS acknowledges 278594-GasAroundGalaxies.

## REFERENCES

- Bacon R., et al., 2010, in *Ground-based and Airborne Instrumentation for Astronomy III*. p. 773508, doi:10.1117/12.856027
- Bacon R., et al., 2015, *A&A*, **575**, A75
- Bertin E., Arnouts S., 1996, *A&AS*, **117**, 393
- Bina D., et al., 2016, *A&A*, **590**, A14
- Blanc G. A., et al., 2011, *ApJ*, **736**, 31

- Borisova E., et al., 2016, preprint, ([arXiv:1605.01422](https://arxiv.org/abs/1605.01422))
- Casertano S., et al., 2000, *AJ*, **120**, 2747
- Cassata P., et al., 2011, *A&A*, **525**, A143
- Cowie L. L., Hu E. M., 1998, *AJ*, **115**, 1319
- Dawson S., Rhoads J. E., Malhotra S., Stern D., Wang J., Dey A., Spinrad H., Jannuzi B. T., 2007, *ApJ*, **671**, 1227
- Dayal P., Libeskind N. I., 2012, *MNRAS*, **419**, L9
- Deharveng J.-M., et al., 2008, *ApJ*, **680**, 1072
- Dijkstra M., Gronke M., Venkatesan A., 2016, preprint, ([arXiv:1604.08208](https://arxiv.org/abs/1604.08208))
- Drake A. B., et al., 2013, *MNRAS*, **433**, 796
- Drake A. B., et al., 2015, *MNRAS*, **454**, 2015
- Dressler A., Martin C. L., Henry A., Sawicki M., McCarthy P., 2011, *ApJ*, **740**, 71
- Dressler A., Henry A., Martin C. L., Sawicki M., McCarthy P., Villaneuva E., 2015, *ApJ*, **806**, 19
- Garel T., Blaizot J., Guiderdoni B., Schaerer D., Verhamme A., Hayes M., 2012, *MNRAS*, **422**, 310
- Garel T., Blaizot J., Guiderdoni B., Michel-Dansac L., Hayes M., Verhamme A., 2015, *MNRAS*, **450**, 1279
- Garel T., Guiderdoni B., Blaizot J., 2016, *MNRAS*, **455**, 3436
- Gronke M., Dijkstra M., Trenti M., Wyithe S., 2015a, *MNRAS*, **449**, 1284
- Gronke M., Bull P., Dijkstra M., 2015b, *ApJ*, **812**, 123
- Hatton S., Devriendt J. E. G., Ninin S., Bouchet F. R., Guiderdoni B., Vibert D., 2003, *MNRAS*, **343**, 75
- Henry A. L., Martin C. L., Dressler A., Sawicki M., McCarthy P., 2012, *ApJ*, **744**, 149
- Hu E. M., Cowie L. L., Capak P., McMahon R. G., Hayashino T., Komiyama Y., 2004, *AJ*, **127**, 563
- Johnston R., 2011, *A&ARv*, **19**, 41
- Konno A., Ouchi M., Nakajima K., Duval F., Kusakabe H., Ono Y., Shimasaku K., 2016, *ApJ*, **823**, 20
- Kurk J. D., Cimatti A., di Serego Alighieri S., Vernet J., Daddi E., Ferrara A., Ciardi B., 2004, *A&A*, **422**, L13
- Matsuda Y., et al., 2012, *MNRAS*, **425**, 878
- Matthee J., Sobral D., Santos S., Röttgering H., Darvish B., Mobasher B., 2015, *MNRAS*, **451**, 400
- Momose R., et al., 2014, *MNRAS*, **442**, 110
- Ouchi M., et al., 2003, *ApJ*, **582**, 60
- Ouchi M., et al., 2008, *ApJS*, **176**, 301
- Rauch M., et al., 2008, *ApJ*, **681**, 856
- Rhoads J. E., Malhotra S., Dey A., Stern D., Spinrad H., Jannuzi B. T., 2000, *ApJ*, **545**, L85
- Santos S., Sobral D., Matthee J., 2016, preprint, ([arXiv:1606.07435](https://arxiv.org/abs/1606.07435))
- Schaerer D., Hayes M., Verhamme A., Teyssier R., 2011, *A&A*, **531**, A12
- Shimasaku K., et al., 2006, *PASJ*, **58**, 313
- Sobral D., et al., 2009, *MNRAS*, **398**, 75
- Sobral D., Smail I., Best P. N., Geach J. E., Matsuda Y., Stott J. P., Cirasuolo M., Kurk J., 2013, *MNRAS*, **428**, 1128
- Tremonti C. A., et al., 2004, *ApJ*, **613**, 898
- Verhamme A., Schaerer D., Maselli A., 2006, *A&A*, **460**, 397
- Wisotzki L., et al., 2016, *A&A*, **587**, A98
- Yamada T., Matsuda Y., Kousai K., Hayashino T., Morimoto N., Umemura M., 2012, *ApJ*, **751**, 29
- Yuma S., et al., 2013, *ApJ*, **779**, 53
- van Breukelen C., Jarvis M. J., Venemans B. P., 2005, *MNRAS*, **359**, 895

flux measured via PLATEFIT, in column 7 the curve of growth flux measured in Wisotzki et al. (2016; where given), column 8 gives the two arcsecond aperture flux estimate from this work, and the 9th column gives the curve of growth flux estimate from this work. All fluxes are quoted in units of  $10^{-18} \text{ergs}^{-1} \text{cm}^{-2}$ . In the 10th, and final, column, we give the diameter of the aperture within which we make the flux measurement in the curve-of-growth analysis.

## APPENDIX A: FLUX CATALOGUE

Table A1 presents various flux estimates for all 59 objects detected automatically with MUSELET. The first column gives the ID of the object in B15. The second and third columns give the RA and DEC coordinates of each detection as found by MUSELET, the fourth column gives the peak wavelength  $\lambda$  of MUSELET's detection, and the fifth column gives the Ly $\alpha$  redshift. The following columns give four different flux estimates for each source, in column 6 the B15

Table A1: Various flux estimates for all 59 objects detected automatically with MUSELET. Column descriptions are given at the beginning of the Appendix.

Bacon ID	RA <sub>MUSELET</sub> (J2000)	DEC <sub>MUSELET</sub> (J2000)	$\lambda_{\text{obs}}$ Å	$z_{\text{Ly}\alpha}$	$10^{-18} \text{ ergs}^{-1} \text{ cm}^{-2}$	Flux <sub>BI5</sub> $10^{-18} \text{ ergs}^{-1} \text{ cm}^{-2}$	Flux <sub>Wisotzki</sub> $10^{-18} \text{ ergs}^{-1} \text{ cm}^{-2}$	Flux <sub>2''</sub> $10^{-18} \text{ ergs}^{-1} \text{ cm}^{-2}$	Flux <sub>C.o.G</sub> $10^{-18} \text{ ergs}^{-1} \text{ cm}^{-2}$	Aperture diameter C.o.G''
43	338.2168	-60.5618	5217.50	3.29	19.90	34.00	15.04±2.61	29.28±5.88	4.04	
71	338.2234	-60.5652	4967.50	3.09	23.01	-	21.87±4.01	30.39±7.34	5.66	
92	338.2283	-60.5706	6783.75	4.58	10.45	22.20	9.70±2.14	16.32±4.29	4.04	
95	338.2441	-60.5691	6350.00	4.22	3.71	12.70	3.58±2.51	9.03±7.64	4.85	
112	338.2396	-60.5635	5967.50	3.91	14.43	26.40	15.65±2.35	29.06±11.84	7.68	
139	338.2310	-60.5611	5288.75	3.35	6.05	19.60	10.20±2.27	26.72±12.83	8.08	
144	338.2455	-60.5666	6098.75	4.02	31.14	-	31.29±4.64	43.51±6.06	4.04	
159	338.2469	-60.5630	5772.50	3.75	4.31	-	5.70±1.61	11.24±5.34	4.04	
162	338.2460	-60.5561	5201.25	3.28	1.29	-	3.51±1.82	4.61±4.64	4.04	
181	338.2462	-60.5571	5273.75	3.34	18.15	27.10	18.62±4.12	28.42±6.50	5.25	
202	338.2473	-60.5685	5201.25	3.28	10.94	-	15.24±2.31	19.94±6.07	4.04	
216	338.2363	-60.5607	6100.00	4.02	6.55	12.90	9.87±1.46	17.10±7.04	5.66	
218	338.2414	-60.5556	7173.75	4.90	2.69	-	3.87±1.34	5.89±3.97	3.64	
225	338.2318	-60.5553	6458.75	4.31	8.72	-	10.42±1.97	13.49±5.82	4.44	
232	338.2191	-60.5610	7557.50	5.22	2.04	4.30	2.56±1.07	3.44±2.45	4.04	
246	338.2350	-60.5584	8121.25	5.68	5.68	12.60	7.12±3.35	11.85±7.24	5.25	
290	338.2425	-60.5612	8618.75	6.09	4.08	-	4.64±2.14	6.19±8.27	4.85	
294	338.2196	-60.5596	6070.00	3.99	3.26	7.30	4.16±1.14	4.87±2.11	2.83	
308	338.2416	-60.5617	6101.25	4.02	2.26	7.60	4.95±1.45	6.33±3.54	3.64	
311	338.2383	-60.5643	5945.00	3.89	3.24	5.00	4.14±1.16	4.49±2.55	3.23	
325	338.2179	-60.5629	6931.25	4.70	6.17	11.50	8.16±1.48	10.89±3.39	4.04	
334	338.2202	-60.5598	7192.50	4.91	2.77	-	3.11±0.90	3.48±1.36	2.83	
338	338.2171	-60.5560	7173.75	4.90	5.74	-	4.04±1.76	3.96±1.30	1.62	
393	338.2414	-60.5581	6308.75	4.19	3.22	7.10	5.92±2.94	14.39±8.94	4.04	
422	338.2173	-60.5697	5021.25	3.13	2.82	6.60	5.09±2.09	5.86±3.61	2.83	
430	338.2331	-60.5644	8855.00	6.28	4.77	-	6.89±2.60	10.12±7.51	4.04	
433	338.2152	-60.5583	5435.00	3.47	7.51	-	9.58±1.67	12.69±5.17	4.04	
437	338.2326	-60.5686	5010.00	3.12	7.38	10.90	7.01±2.45	10.14±4.46	4.04	
441	338.2279	-60.5651	6923.75	4.69	6.54	-	5.78±1.54	7.88±3.09	3.64	
449	338.2437	-60.5672	5200.00	3.28	3.59	-	4.94±1.53	4.82±1.53	2.02	
453	338.2298	-60.5647	6933.75	4.70	1.46	-	1.64±0.72	1.18±1.24	2.83	
462	338.2392	-60.5607	8021.25	5.60	3.68	-	1.37±2.18	1.35±2.69	2.42	
469	338.2340	-60.5643	5431.25	3.47	2.64	-	2.88±1.20	4.97±5.00	4.04	
478	338.2160	-60.5577	5435.00	3.47	2.41	-	3.03±1.75	7.28±9.27	5.66	
484	338.2441	-60.5702	7190.00	4.91	2.94	-	2.90±0.96	3.03±1.32	2.42	
489	338.2377	-60.5623	4810.00	2.96	2.65	-	4.76±1.76	5.98±3.20	2.83	
492	338.2411	-60.5662	8221.25	5.76	2.88	5.10	4.06±1.41	5.34±3.81	4.04	
498	338.2479	-60.5693	6330.00	4.21	3.61	-	4.18±1.76	4.73±3.06	2.83	
499	338.2279	-60.5651	6923.75	4.69	6.40	-	5.78±1.54	7.88±3.09	3.64	
500	338.2364	-60.5656	5475.00	3.50	1.85	-	2.45±1.62	2.38±3.49	3.64	

Table A1: Various flux estimates for all 59 objects detected automatically with MUSELET. Column descriptions are given at the beginning of the Appendix.

Bacon ID	RA <sub>MUSELET</sub> (J2000)	DEC <sub>MUSELET</sub> (J2000)	$\lambda_{\text{obs}}$ <sub>MUSELET</sub> Å	$z_{\text{Ly}\alpha}$	Flux <sub>B15</sub> $10^{-18} \text{ ergs}^{-1} \text{ cm}^{-2}$	Flux <sub>Wisotzki</sub> $10^{-18} \text{ ergs}^{-1} \text{ cm}^{-2}$	Flux <sub>2//</sub> $10^{-18} \text{ ergs}^{-1} \text{ cm}^{-2}$	Flux <sub>C.o.G</sub> $10^{-18} \text{ ergs}^{-1} \text{ cm}^{-2}$	Aperture diameter C.o.G//
503	338.2350	-60.5640	5287.50	3.35	3.43	-	2.99 ± 1.59	3.52 ± 2.44	2.83
513	338.2478	-60.5589	5202.50	3.28	3.09	-	3.01 ± 2.22	5.87 ± 10.62	4.85
546	338.2238	-60.5614	8162.50	5.71	3.80	8.00	6.40 ± 1.35	9.06 ± 3.95	3.64
547	338.2247	-60.5683	8161.25	5.71	3.56	10.70	6.52 ± 1.23	9.71 ± 4.19	4.04
549	338.2318	-60.5613	6900.00	4.67	2.38	4.90	3.95 ± 1.18	4.13 ± 1.70	2.42
551	338.2296	-60.5670	5083.75	3.18	4.04	-	5.13 ± 1.45	6.59 ± 6.76	5.25
552	338.2218	-60.5630	7392.50	5.08	1.76	-	2.05 ± 1.67	2.01 ± 2.56	2.83
553	338.2193	-60.5655	7392.50	5.08	4.69	9.30	6.53 ± 1.50	11.00 ± 7.26	6.46
555	338.2398	-60.5651	6700.00	4.51	1.05	-	2.44 ± 1.24	5.64 ± 4.71	4.85
557	338.2240	-60.5633	7542.50	5.20	1.90	-	2.71 ± 1.21	2.76 ± 2.62	3.23
558	338.2267	-60.5672	5018.75	3.13	2.85	6.10	3.78 ± 1.22	6.20 ± 5.38	5.25
560	338.2464	-60.5568	8363.75	5.88	5.38	-	6.58 ± 1.60	8.51 ± 2.29	2.83
561	338.2155	-60.5610	7065.00	4.81	1.78	-	2.50 ± 1.08	2.47 ± 1.38	2.42
563	338.2182	-60.5669	5868.75	3.83	3.68	6.60	3.54 ± 1.74	4.25 ± 5.94	4.44
568	338.2240	-60.5598	6886.25	4.66	3.42	4.60	4.63 ± 1.29	6.03 ± 4.88	4.44
573	338.2478	-60.5703	8842.50	6.27	2.64	-	4.68 ± 3.80	4.67 ± 3.16	1.62
577	338.2419	-60.5670	8221.25	5.76	6.55	-	9.68 ± 1.35	13.90 ± 3.62	4.04
578	338.2296	-60.5670	5083.75	3.18	2.75	-	5.13 ± 1.45	6.59 ± 6.76	5.25
585	338.2389	-60.5631	5275.00	3.34	2.55	-	2.19 ± 1.26	2.81 ± 1.97	2.83